Electronic Supplementary Material (ESI) for Journal of Materials Chemistry A.

Supporting Information

Chemicals and reagents

Copper foam (1 mm) was obtained from GJY Electron. Mater. Co., Ltd. $Ni(NO_3)_2{\cdot}6H_2O$, $CO(NH_2)_2$, NH_4F, $Na_2WO_4{\cdot}2H_2O$, Na_3VO_4, $Na_2MoO_4{\cdot}2H_2O$, $Fe(NO_3)_3{\cdot}9H_2O$, and C_2H_5OH were obtained from Sinopharm Chemical Reagent Co., Ltd. Pt/C (platinum, 20% on carbon) was supplied by Alfa Aesar. Nafion was obtained from Sigma-Aldrich. All chemicals were analytical reagent grade and used directly. The aqueous solution is prepared by using deionized water (DIW, 18.25 MΩ·cm)

Preparation of $Ni(OH)_2$ NSs and tungstate-intercalated $Ni(OH)_2$ (W-$Ni(OH)_2$) NSs

First, Cu foam (3 × 3 cm^2, 1 mm) was cleaned with ethanol and DIW in the ultrasonic generator for several times and dried in air. Subsequently, seal Cu foam into a 100 mL Teflon autoclave filled with 80 mL of the aqueous solution containing 3.2 mmol $Ni(NO_3)_2{\cdot}6H_2O$, 16 mmol $CO(NH_2)_2$, and 7.7 mmol NH_4F and place the Teflon autoclave in an oven at 120 °C for 2 h. After the reaction, take out the sample, clean it with ethanol and DIW for a few times, and dry it in air. For W-$Ni(OH)_2$ NSs, the molar ratio of W/Ni (n_W/n_{Ni} = 1/20, 1/10, and 1/5) is manipulated by controlling the different dosage of $Na_2WO_4{\cdot}2H_2O$. Samples with W/Ni mole ratios of 1/20, 1/10, and 1/5 were labeled as W-5 %-$Ni(OH)_2$ NSs, W-$Ni(OH)_2$ NSs, and W-20 %-$Ni(OH)_2$ NSs, respectively.

Preparation of Cu_xO@$Ni(OH)_2$, Cu_xO@W-$Ni(OH)_2$, Cu_xO@Mo-$Ni(OH)_2$, and Cu_xO@V-$Ni(OH)_2$

The $Cu(OH)_2$ nanorod is generated via a typical chemical oxidation method based on the previous literature.[1] The synthesis procedure of Cu_xO@$Ni(OH)_2$ was almost the same as the synthesis process of $Ni(OH)_2$ NSs except replacing Cu foam with $Cu(OH)_2$/Cu foam. Due to the reduction effect of urea, $Cu(OH)_2$ was reduced to the mixed phase of Cu_2O and CuO (denoted as Cu_xO). As for Cu_xO@W-$Ni(OH)_2$, Cu_xO@Mo-$Ni(OH)_2$, and Cu_xO@V-$Ni(OH)_2$, additional 0.106 g of $Na_2WO_4{\cdot}2H_2O$, 0.077 g of $Na_2MoO_4{\cdot}2H_2O$, and 0.058 g of Na_3VO_4, respectively, into the system.

Preparation of NNH NSs, NWNH NSs, Cu_2O@NNH, Cu_2O@NWNH, Cu_2O@NMoNH, and Cu_2O@NVNH

The H_2 plasma strategy reported in our previous work was employed to fabricate the NNH heterostructure.[2] The detailed parameters are listed below: pressure of H_2: 40 Pa; activation time: 20 min; plasma power: 400 W. Notably, due to the reduction effect of H_2 plasma, Cu_xO was totally reduced to Cu_2O.

Material characterizations

We carried out X-ray diffraction (XRD) analysis on X-pert Powder. Scanning electron microscopy (SEM) was performed on Hitachi SU 8010. The JEOL JEM-2100 F was chosen to perform Transmission electron microscopy (TEM). We carried out the high-resolution transmission electron microscopy (HRTEM) on the same equipment with TEM. So did selected area electron diffraction (SAED). NICOTCT was used to conduct Fourier transform infrared (FT-IR) test. Raman spectra were recorded on a DXR SmartRaman with a 522 nm laser as an excitation source. Thermo Scientific ESCALAB 250Xi was used to collect on the data of X-ray photoelectron spectroscopy (XPS). The C 1s peak at 284.8 eV was used to calibrate the XPS data. The proportion of metal elements was measured by Inductively coupled plasma-mass spectrometry (ICP-MS) measurement (ICAPQ). The water contact angles were measured by contact angle analyzer (SL200B, Solon Tech).

Electrochemical characterizations

The electrochemical tests were conducted on a CHI 760 workstation using a Ag/AgCl reference electrode and a carbon counter electrode. The as-synthesized materials were used as a working electrode. 1.0 M PBS (pH = 6.97) was used as the electrolyte. All linear sweep voltammograms (LSVs) curves were *iR*-corrected (95 %) and measured at a scan rate of 0.005 V s^{-1}. The calculation of electrochemical impedance spectroscopy (EIS), electrochemical active surface area (ECSA), and Faradic efficiency were based on our previous work.[2] The chronoamperometry (CA) tests are carried out under constant voltages for stability tests. The turnover frequency (TOF) values are estimated according to the equation: TOF = $I/2NF$, where I is current (A), the factor 1/2 arrives from two electrons needed to form one hydrogen molecule, N is the total number of active sites, and F is Faraday constant (96,485 C mol^{-1}). The N value is calculated according to the equation: $n = Q/2F = (I*t)/2F = (I*V/\mu)/2F = S/(2F*\mu)$, where S is integrated effective area in CV recorded, and μ is the scan rate (50 mV s^{-1}).

Theoretical Calculations

All computations were conducted by spin-polarized density functional theory (DFT) using the VASP.[3] By the way of expanding the wave function of valence electrons, we set a plane-wave basis with a kinetic-energy cut-off of 400 eV. The generalized gradient approximation (GGA) and the Perdew-Burke-Ernzerhof (PBE) functional were employed.[4] The total energy range was set to be 10^{-4} eV. The force convergences were 0.03 eV/Å. We combined $Ni(OH)_2$ nanosheet and Ni nanocluster to module the complex structures. The $Ni(OH)_2$ was modified by CO_3 and WO_4. To avoid the interaction between the adjacent layers, we set 20 Å vacuum space between sheets. The 3 × 3 × 1 k-points Monkhorst-Pack mesh was used to sample the Brillouin-zone integration.

The computational hydrogen electrode (CHE) proposed by Norskov et al. was used to explore the HER activity of the electrocatalysts.[5] The Gibbs free energy of the intermediates adsorbed on catalyst (GM) is obtained by equation 1:

$$\Delta G_{M} = \Delta E_{M*} + \Delta ZPE - T\Delta S \qquad (1)$$

where $\Delta EM*$, ΔZPE, and ΔS are the binding energy, zero-point energy change, and entropy change of intermediates adsorption, respectively. Herein, the value of ΔZPE and TΔS were calculated by Norskov et al.8 and ΔEM* is calculated using equation 2:

$$\Delta E_{\mathrm{M}*} = E_{\mathrm{M}*} - E_{*} - E_{\mathrm{M}} \qquad (2)$$

where EM* and E* are the total energy of basal surface with and without intermediates M (H2O, H, H2), respectively. EM is the energy of intermediate M.

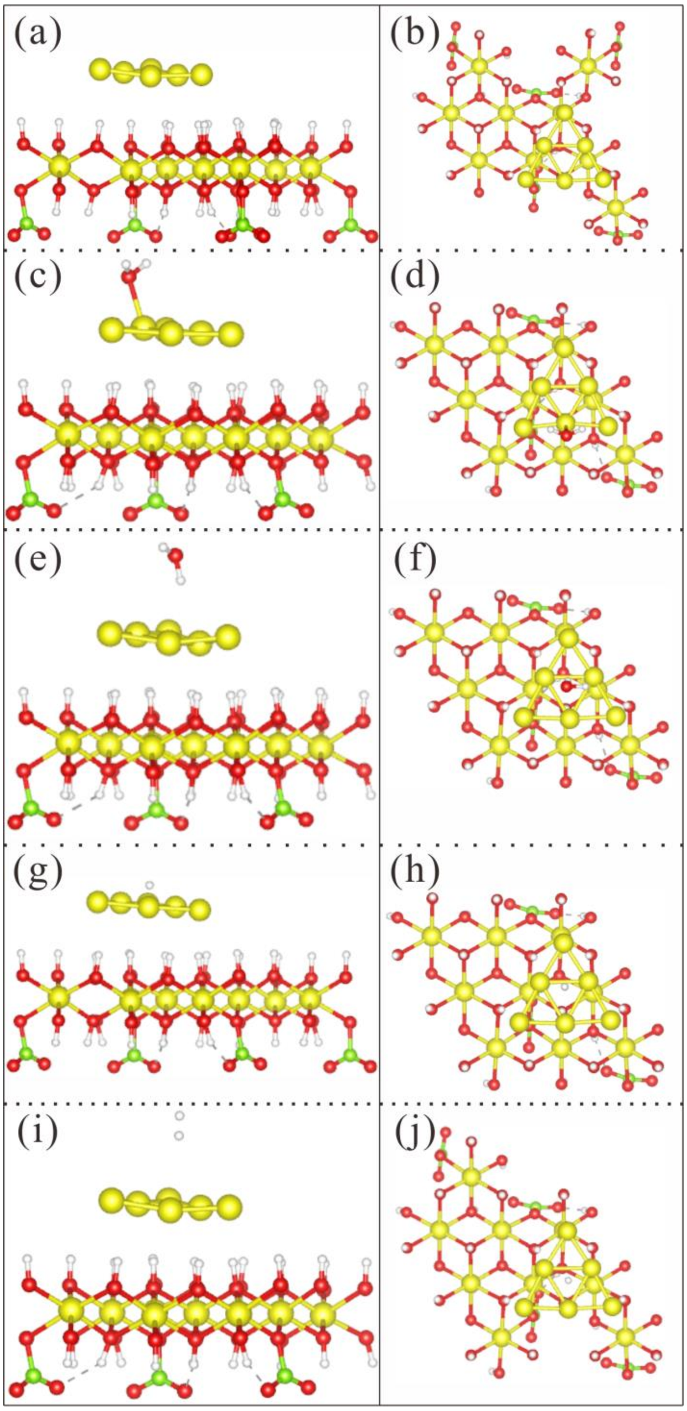

Figure S1. The Side view and top view of the model of NNH (a-b), the water adsorption (c-d), the water dissociation (e-f), H adsorption (g-h) and H_2 desorption (i-j) on NNH interface. Yellow balls: Ni atoms; Red balls: O atoms; White balls: H atoms; Green balls: C atoms.

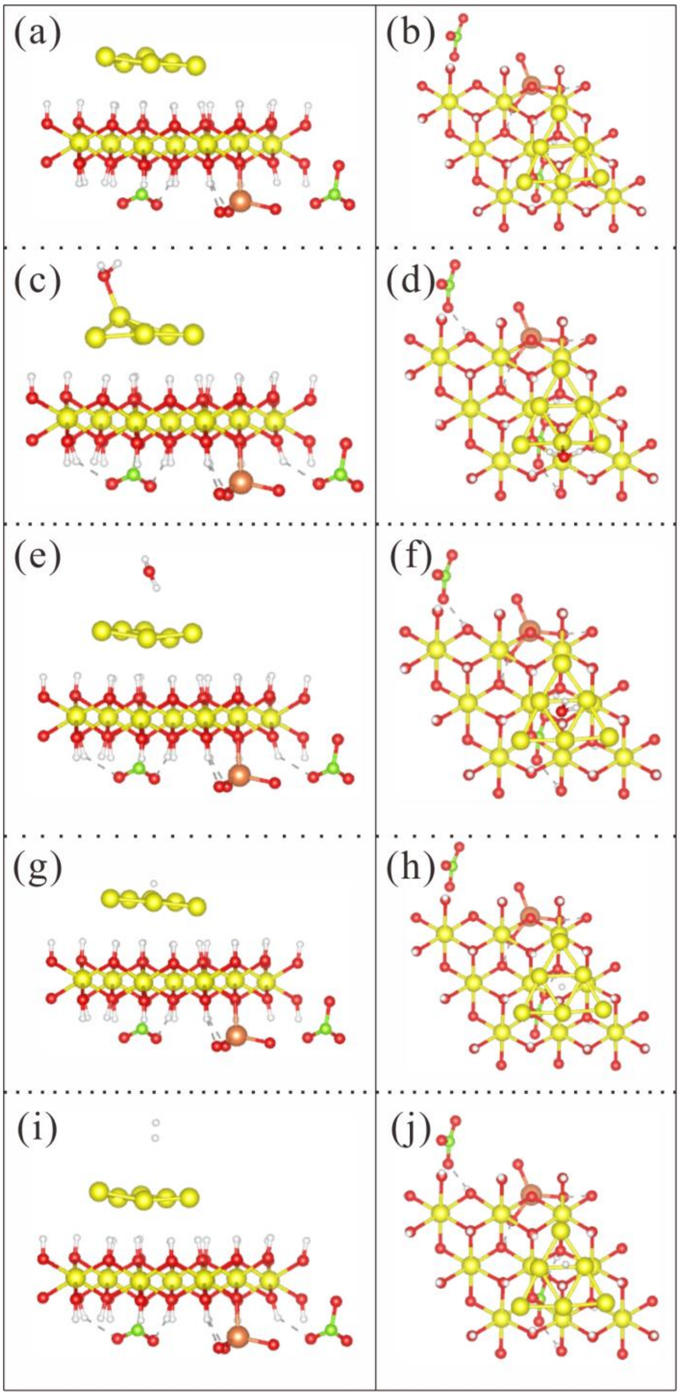

Figure S2. The Side view and top view of the model of NWNH (a-b), the water adsorption (c-d), the water dissociation (e-f), H adsorption (g-h) and H_2 desorption (i-j) on NWNH interface. Yellow balls: Ni atoms; Red balls: O atoms; White balls: H atoms; Green balls: C atoms; Orange ball: W atom.

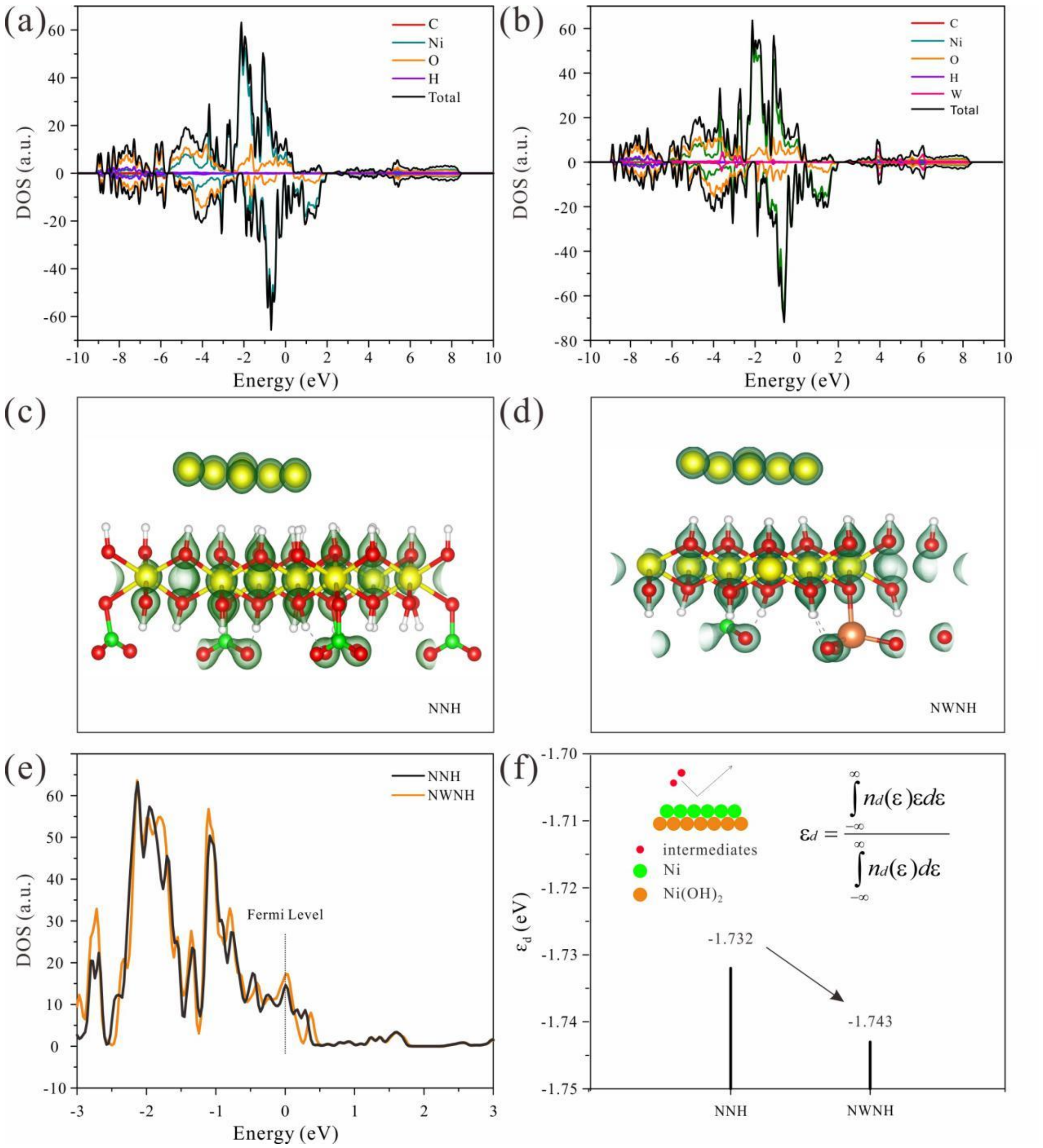

Figure S3. The DOS of (a) NNH and (b) NWNH. The charge distribution of (c) NNH and (d) NWNH. Yellow balls: Ni atoms; Red balls: O atoms; White balls: H atoms; Green balls: C atoms; Orange ball: W atom. (e) The DOS comparison of NNH and NWNH. (f) The d-band center of NNH and NWNH. The ε is the electron energy, $n_d(\varepsilon)$ is the density of electron.

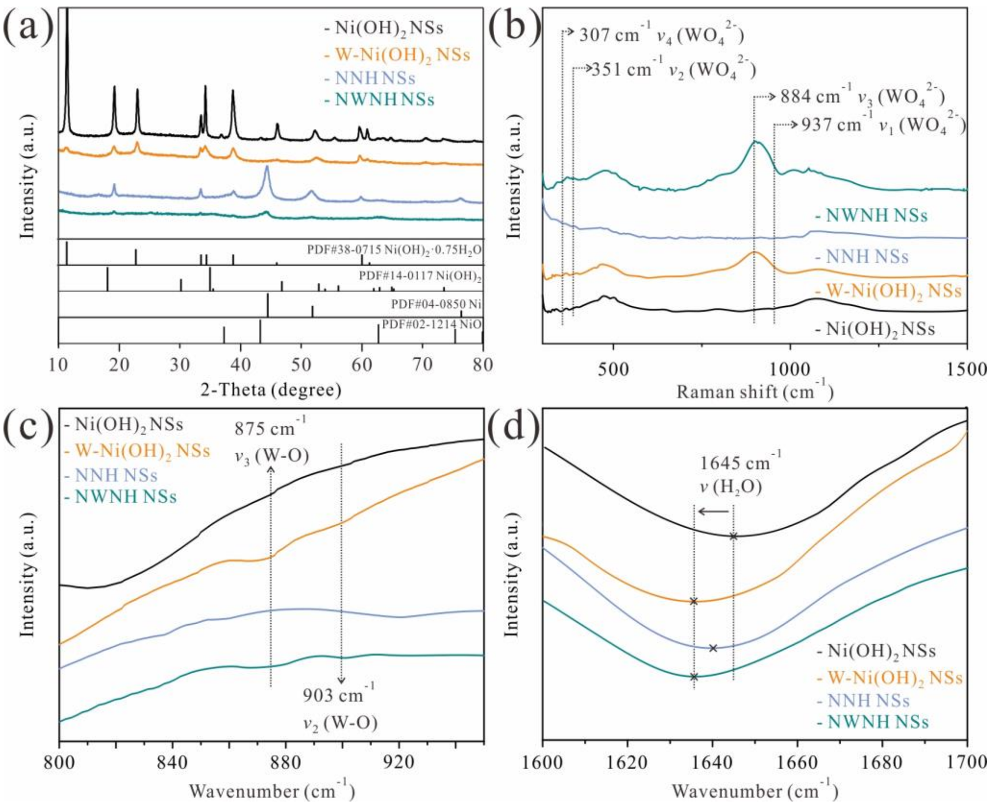

Figure S4. (a) XRD patterns, (b) Raman spectra, and (c,d) FT-IR spectra of Ni(OH)$_2$ NSs, W-Ni(OH)$_2$ NSs, NNH NSs, and NWNH NSs. The two bands at 875 cm^{-1} and 903 cm^{-1} in the W-incorporated materials represent v_1(W-O) and v_3(W-O), respectively.[6] The W-incorporated samples also exhibit strong characteristic peaks at 307, 351, 884, and 937 cm^{-1} in Raman spectra, corresponding to the internal patterns of the v_1, v_2, v_3, and v_4 of WO$_4^{2-}$ tetrahedron, respectively.[7]

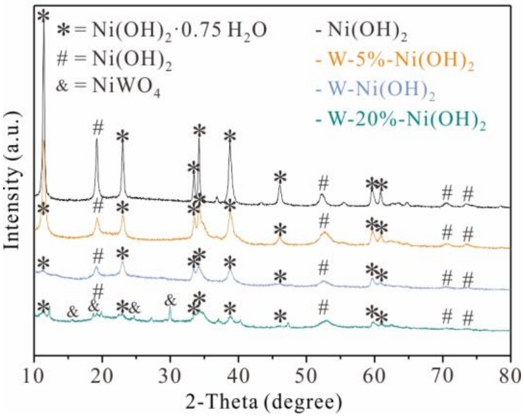

Figure S5. XRD patterns of Ni(OH)$_2$ NSs, W-5%-Ni(OH)$_2$ NSs, W-Ni(OH)$_2$ NSs, and W-20%-Ni(OH)$_2$ NSs. It is noted that no additional diffraction peaks associated with other phase emerge when the mole radios of W to Ni are 5 % and 10 %. However, when the ratio of W to Ni increases to 20 %, the characteristic peaks of NiWO$_4$ occur. The appearance of NiWO$_4$ indicates when the amount of introduced WO$_4^{2-}$ exceeds the inserted limitation between layers, the overflowing WO$_4^{2-}$ tends to react with Ni^{2+} to form NiWO$_4$.

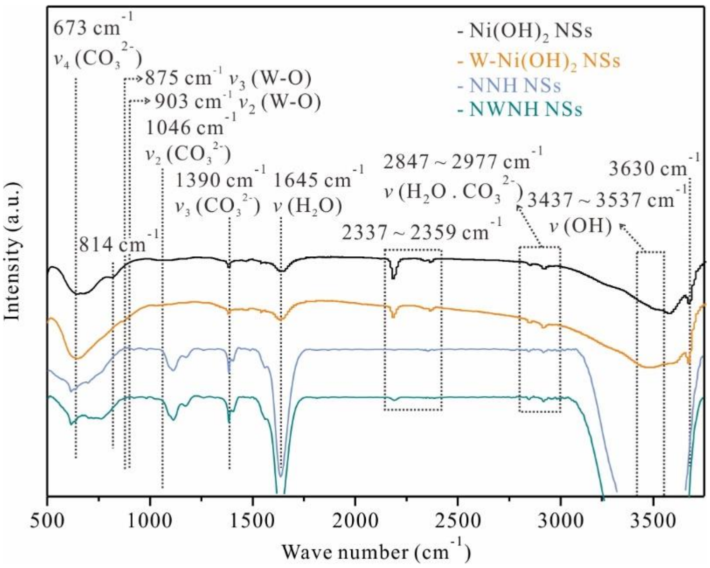

Figure S6. The whole FT-IR spectra of Ni(OH)$_2$ NSs, W-Ni(OH)$_2$ NSs, NNH NSs, and NWNH NSs.

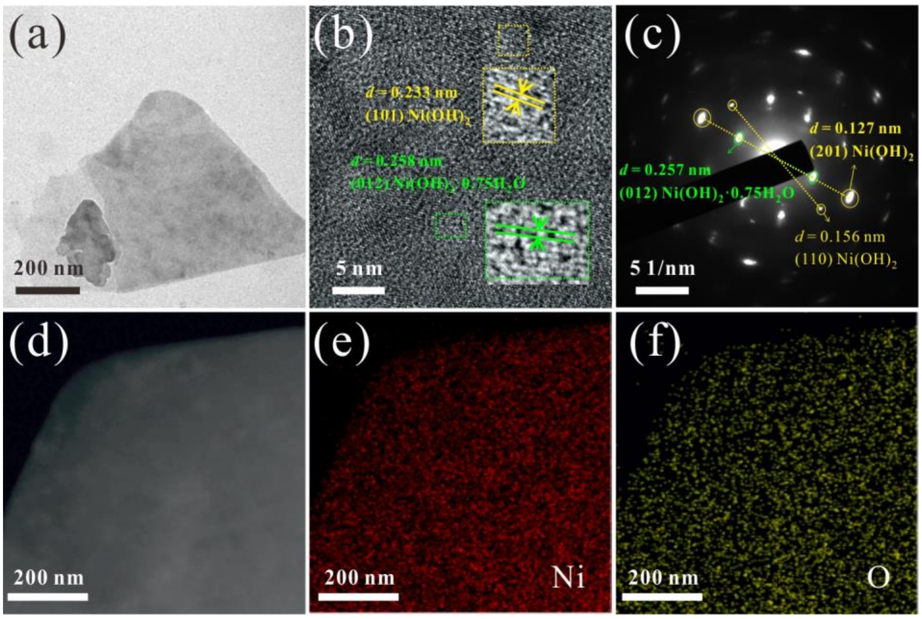

Figure S7. (a) TEM image, (b) HRTEM image, and (c) SAED pattern of Ni(OH)$_2$ NSs. (d-f) HAADF-STEM image and corresponding elemental mapping images of Ni(OH)$_2$ NSs.

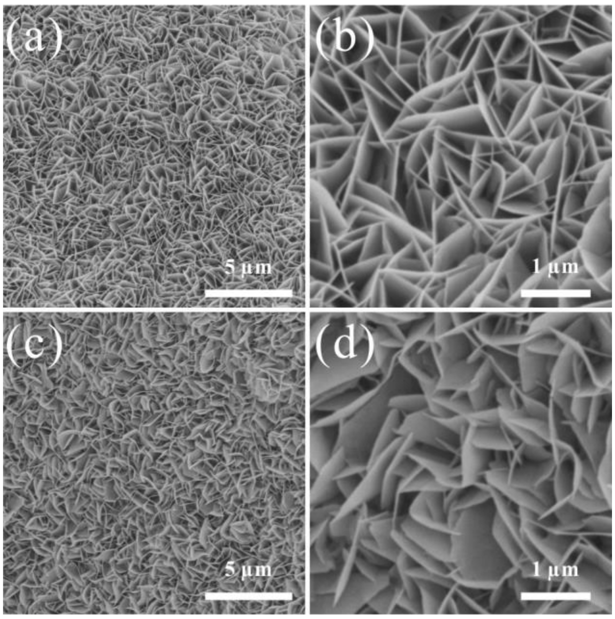

Figure S8. SEM images of W-5 %-$Ni(OH)_2$ NSs (a,b) and W-20 %-$Ni(OH)_2$ NSs (c,d).

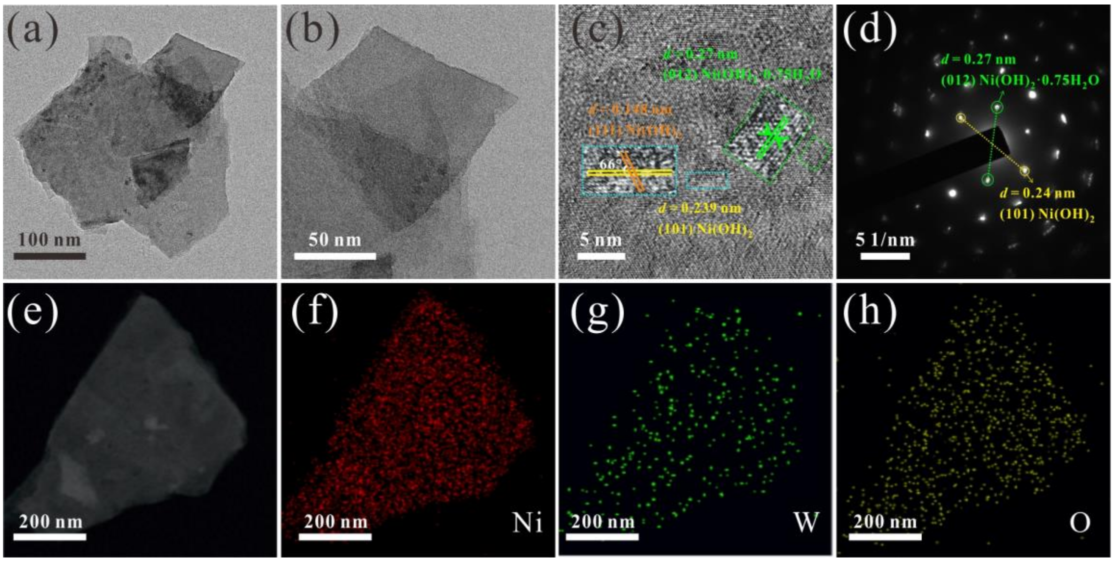

Figure S9. (a-b) TEM images, (c) HRTEM image, and (d) SAED pattern of W-$Ni(OH)_2$ NSs. (e-h) HAADF-STEM image and corresponding elemental mapping images of W-$Ni(OH)_2$ NSs.

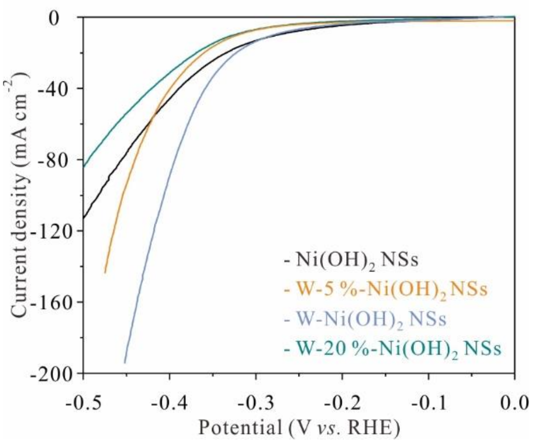

Figure S10. (a) LSV curves of $Ni(OH)_2$ NSs, W-5 %-$Ni(OH)_2$ NSs, W-$Ni(OH)_2$ NSs, and W-20 %-$Ni(OH)_2$ NSs in 1.0 M PBS.

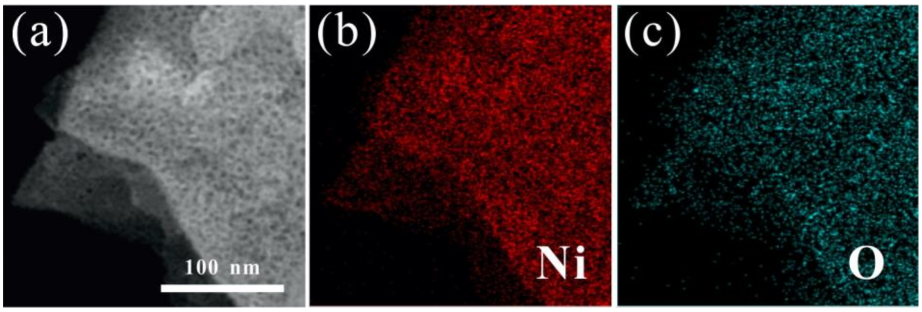

Figure S11. (a-c) HAADF-STEM image and corresponding elemental mapping images of NNH NSs.

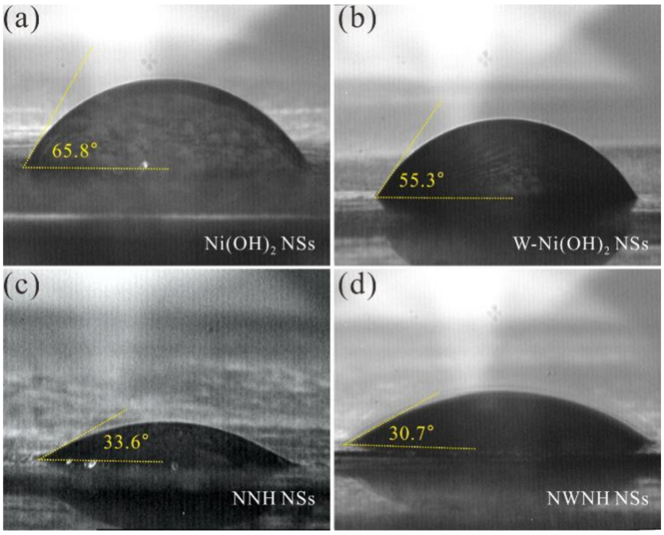

Figure S12. The water contact angles of (a) $Ni(OH)_2$ NSs, (b) W- $Ni(OH)_2$ NSs, (c) NNH NSs, and (d) NWNH NSs. The porous Cu foam is not suitable to perform the tests of contact angles. Thus, the copper sheet is applied as substrate to grow the nanosheets and used for analyzing water contact angle.

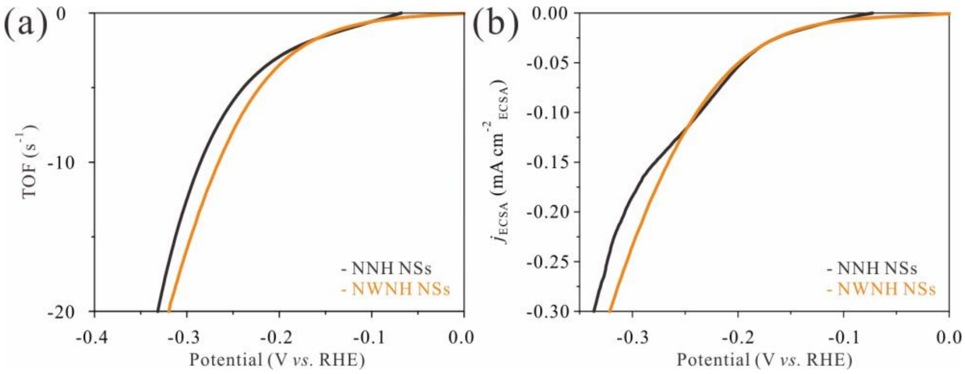

Figure S13. (a) TOF curves and (b) ECSA normalized LSV curves of NNH NSs and NWNH NSs.

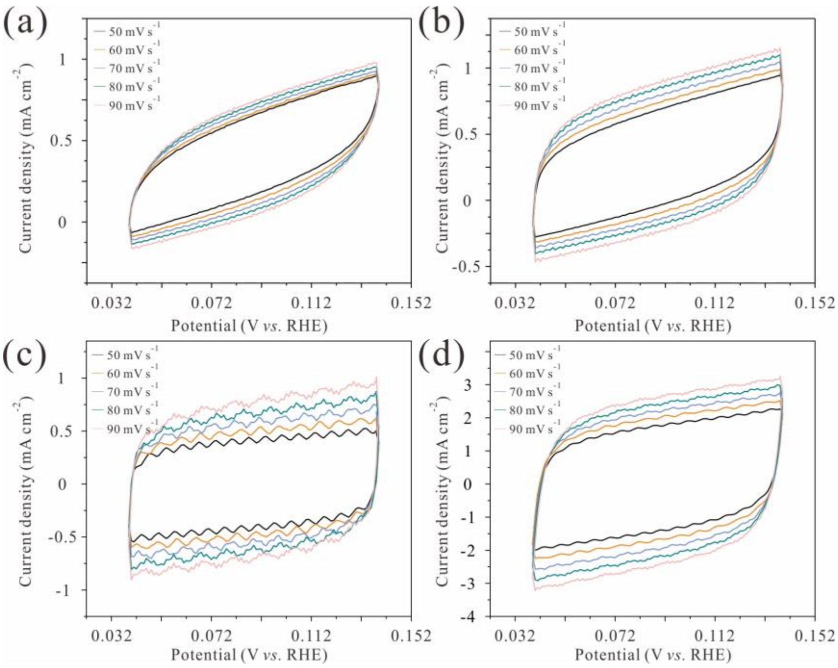

Figure S14. CV curves of (a) $Ni(OH)_2$ NSs, (b) W-$Ni(OH)_2$ NSs, (c) NNH NSs, and (d) NWNH NSs in the double layer capacitive region at different scan rates.

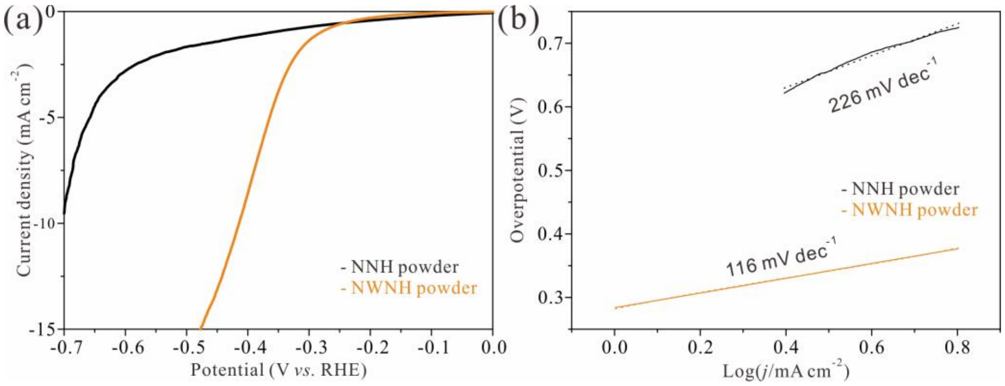

Figure S15. (a) LSV curves, (b) Tafel plots of NNH powder and NWNH powder.

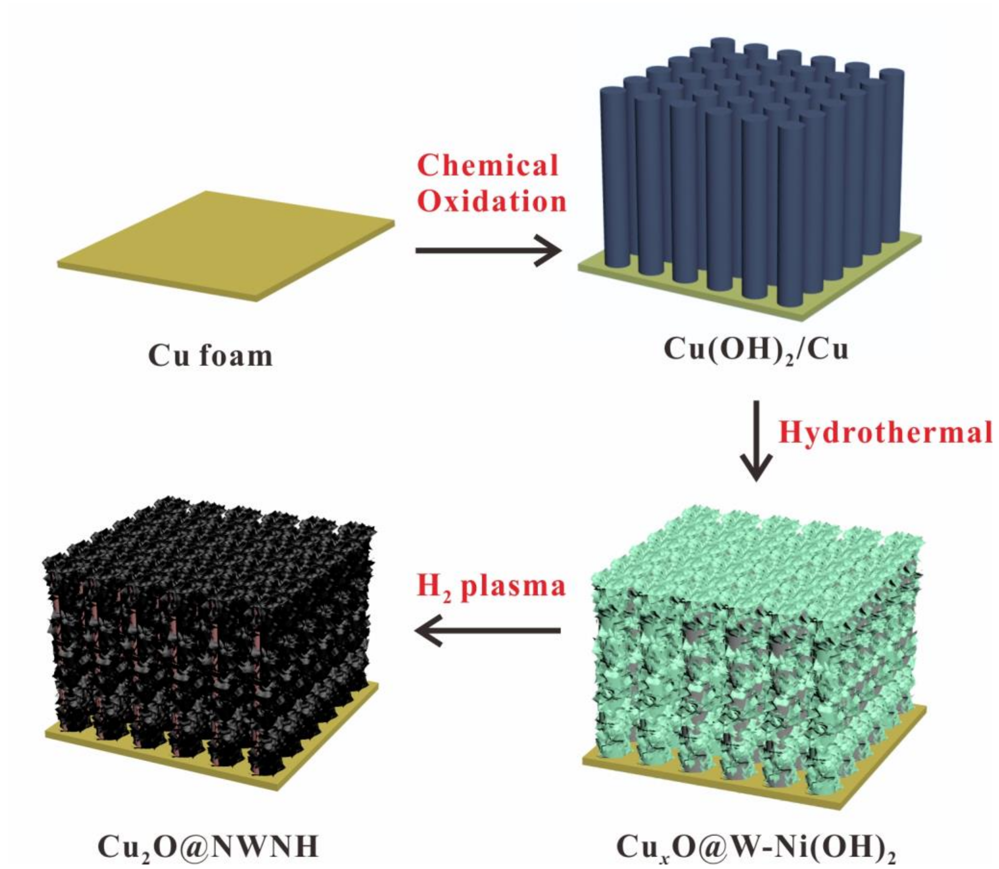

Figure S16. Schematic illustration of the fabrication process of Cu$_2$O@NWNH.

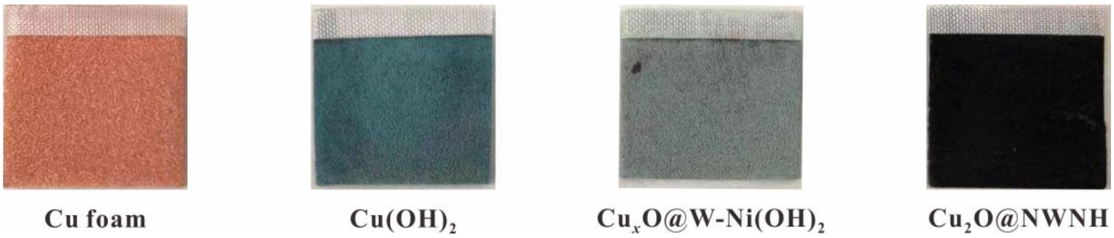

Figure S17. Digital graphs of Cu foam, Cu(OH)$_2$, Cu$_x$O@W-Ni(OH)$_2$, and Cu$_2$O@NWNH.

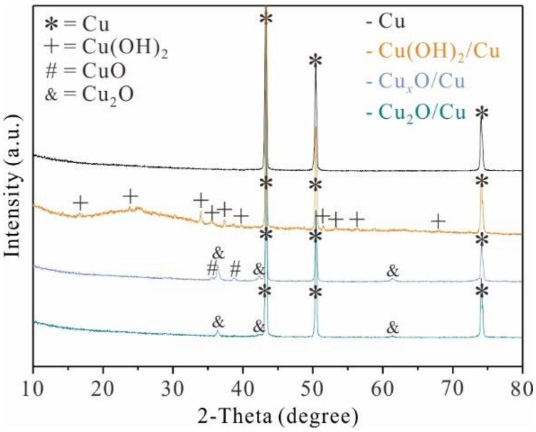

Figure S18. XRD patterns of Cu-based substrate during the reaction.

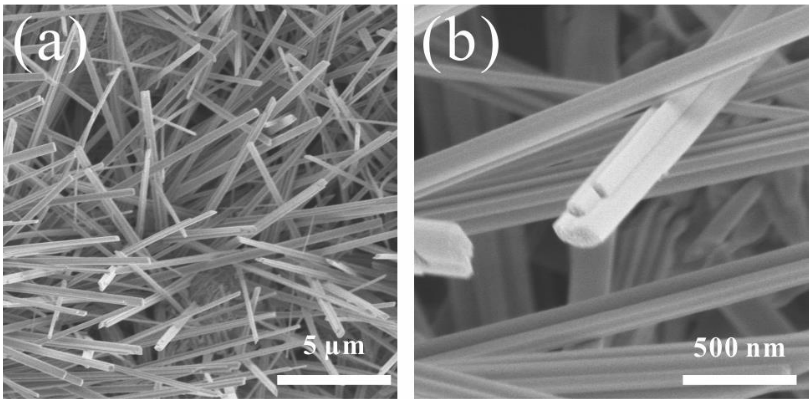

Figure S19. SEM images of Cu(OH)$_2$/Cu substrate.

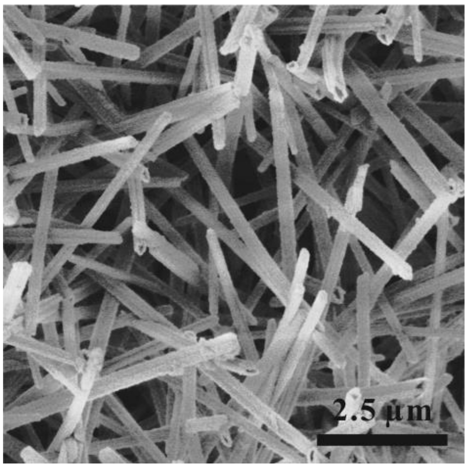

Figure S20. SEM image of Cu$_x$O nanotubes

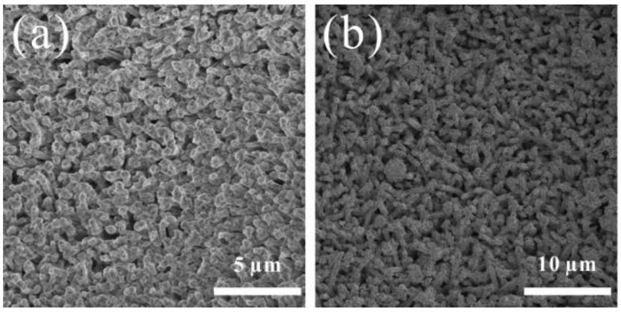

Figure S21. SEM images of (a) Cu$_x$O@W-Ni(OH)$_2$ and (b) Cu$_2$O@NWNH.

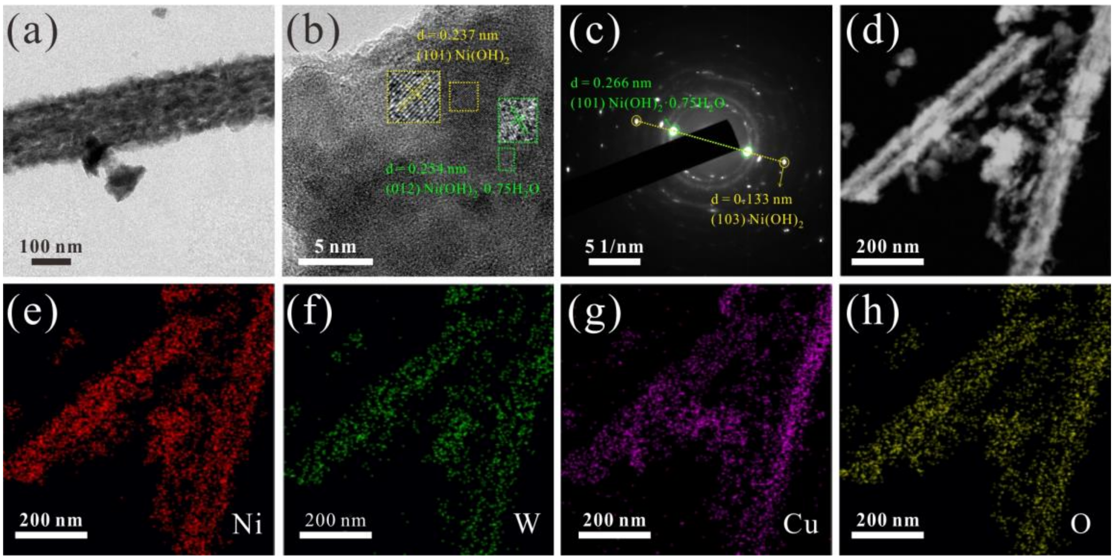

Figure S22. (a) TEM image, (b) HRTEM image, and (c) SAED pattern of Cu$_x$O@W-Ni(OH)$_2$. (d-h) HAADF-STEM image and corresponding elemental mapping images of Cu$_x$O@W-Ni(OH)$_2$.

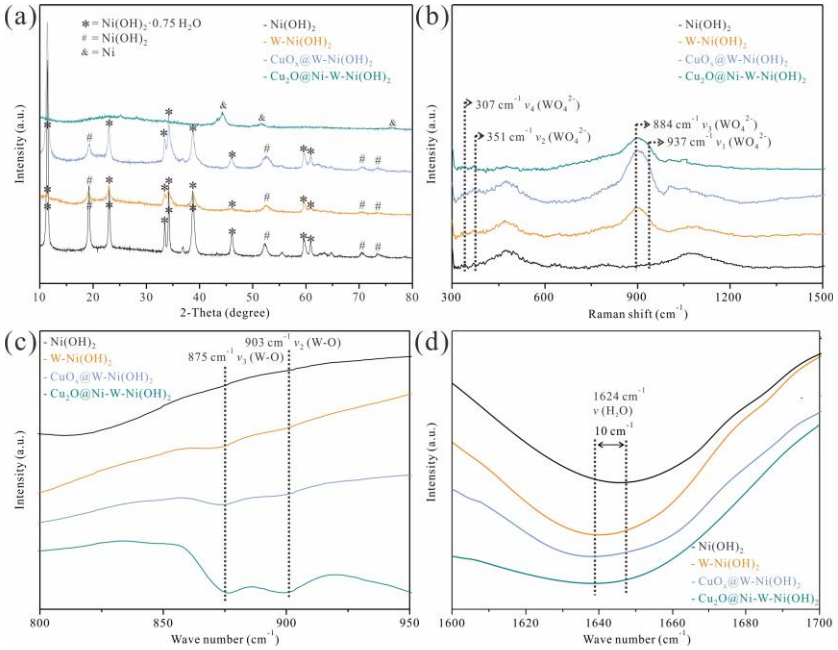

Figure S23. (a) XRD patterns, (b) Raman spectra and (c,d) FT-IR spectra of $Ni(OH)_2$ NSs, W-$Ni(OH)_2$ NSs, Cu_xO@Ni-$Ni(OH)_2$, and Cu_2O@Ni-W-$Ni(OH)_2$.

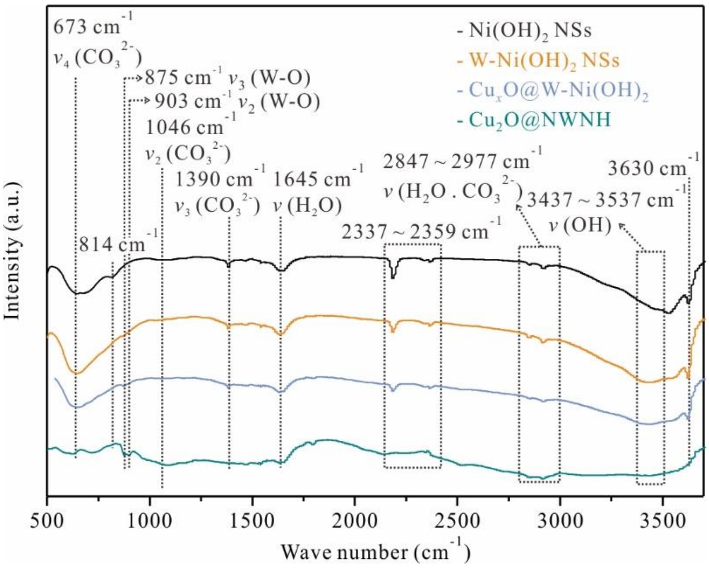

Figure S24. The whole FT-IR spectra of $Ni(OH)_2$ NSs, W-$Ni(OH)_2$ NSs, Cu_xO@Ni-$Ni(OH)_2$, and Cu_2O@NWNH.

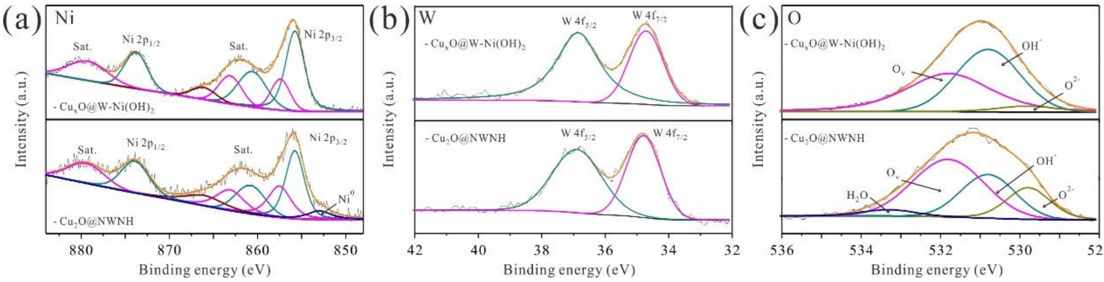

Figure S25. (a-c) The high-resolution Ni 2p (a), W 4f (b), and O 1s (c) XPS spectra of Cu_xO@W-$Ni(OH)_2$ and Cu_2O@NWNH.

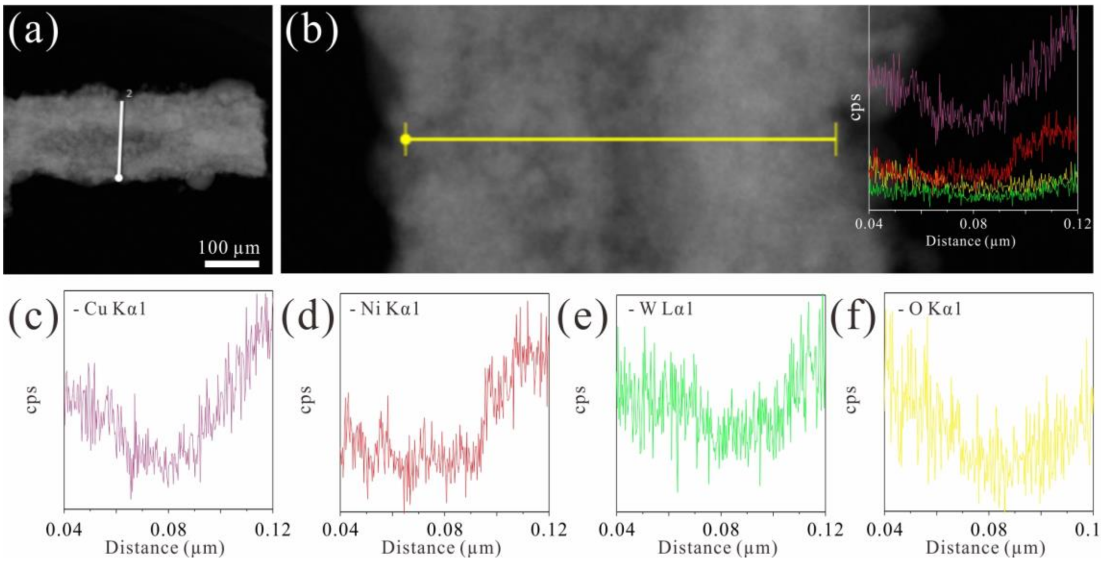

Figure S26. (a,b) The TEM images of Cu_2O@NWNH selected for EDS line scan. The distribution of Cu (c), Ni (d), W (e), and O (f) along line. The inset of (b) is the whole elemental distribution along line.

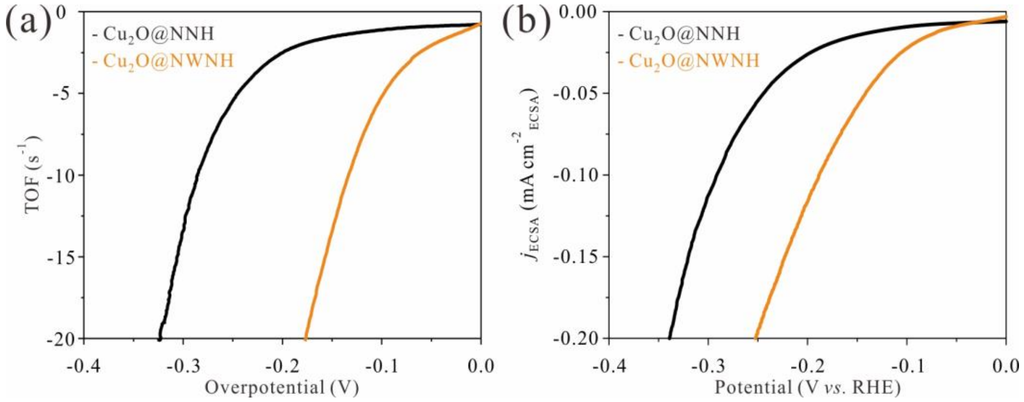

Figure S27. (a) TOF curves and (b) ECSA normalized LSV curves of Cu_2O@NNH and Cu_2O@NWNH.

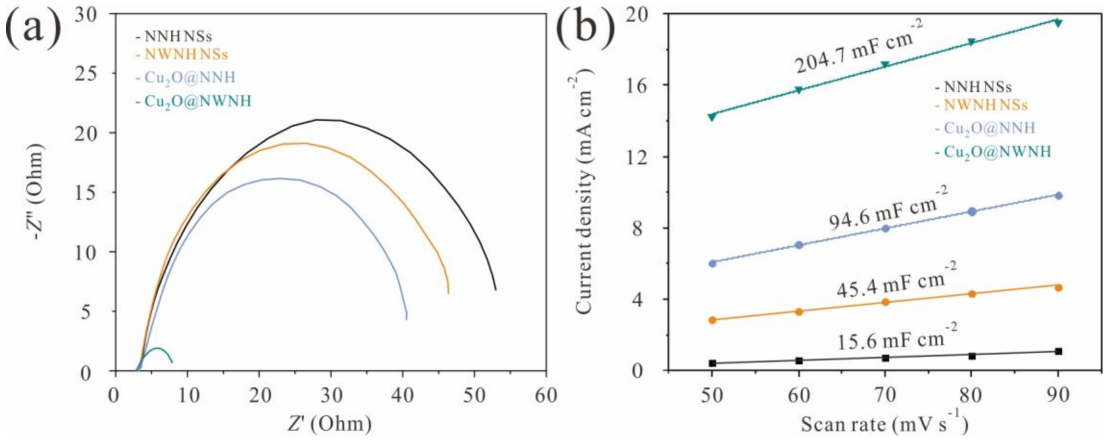

Figure S28. (a) Nyquist plots and (b) capacitive currents as a function of scan rates for NNH NSs, NWNH NSs, Cu_2O@NNH, and Cu_2O@NWNH.

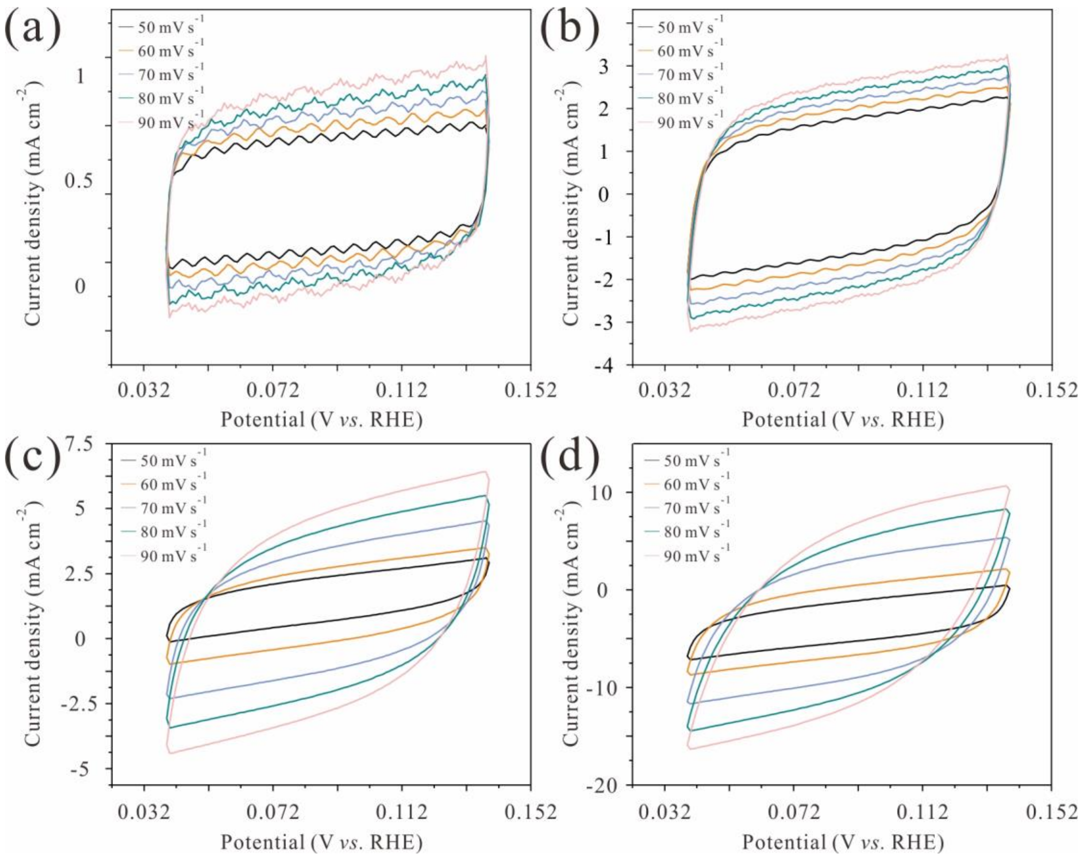

Figure S29. CV curves of (a) NNH NSs, (b) NWNH NSs, (c) Cu_2O@NNH, and (d) Cu_2O@NWNH in the double layer capacitive region at different scan rates.

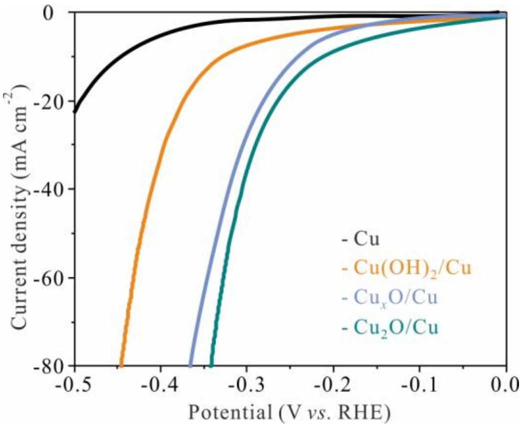

Figure S30. (a) LSV curves of Cu-based substrates in 1 M PBS.

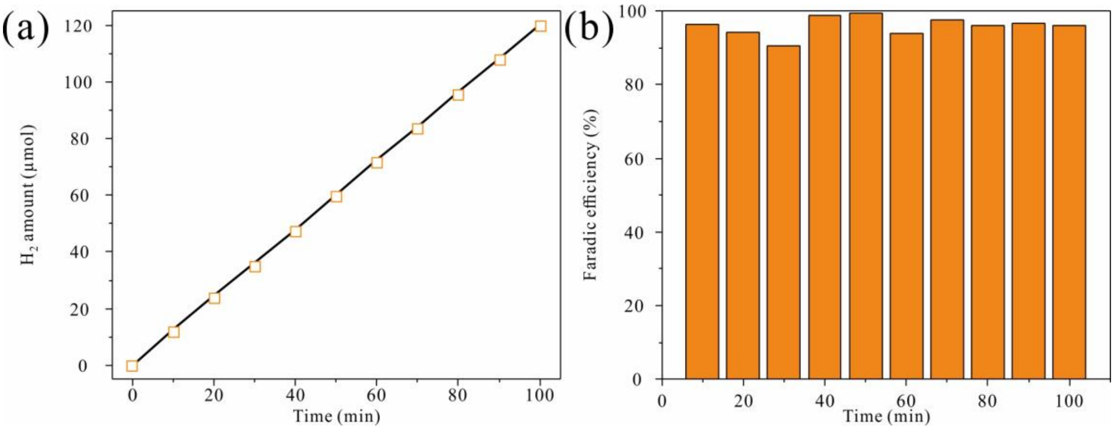

Figure S31. The gas chromatogram of Cu_2O@NWNH in 100 min. (b) Faradaic efficiency and (c) gas yield of hydrogen evolution on the Cu_2O@NWNH as a function of time at the current density of 10 mA cm^{-2}.

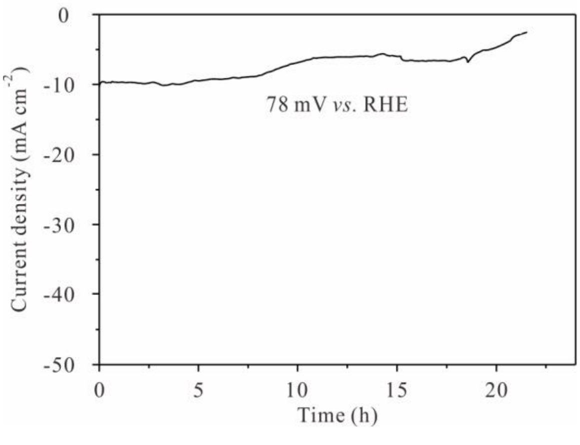

Figure S32. CA test of Cu_2O@NNH.

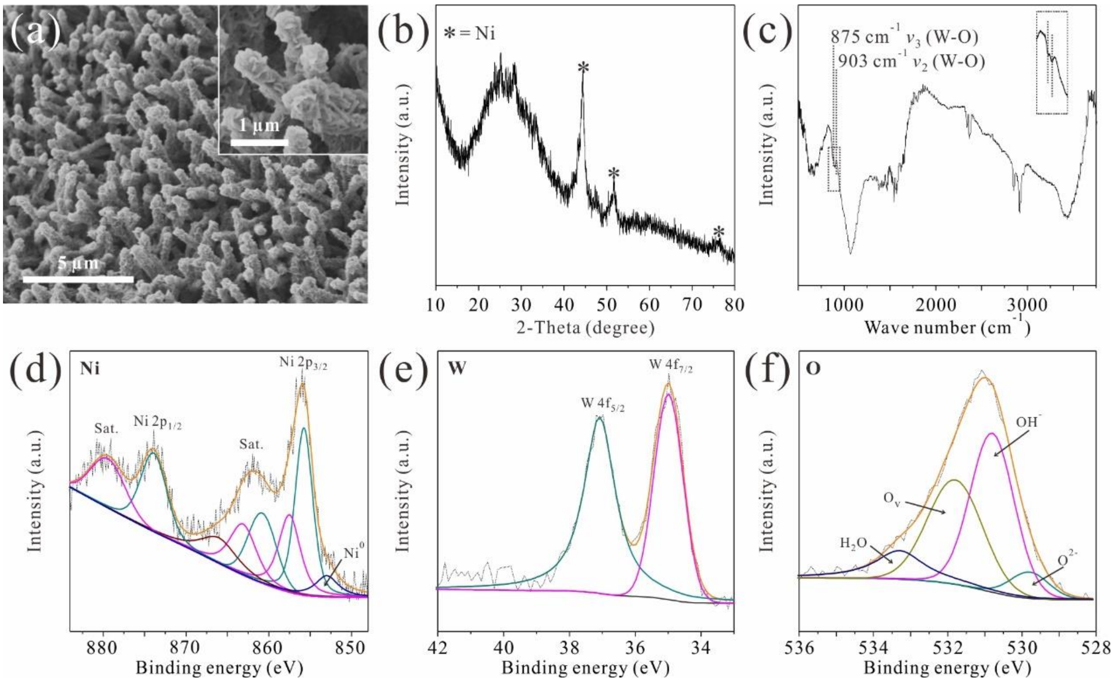

Figure S33. (a) SEM image, (b) XRD pattern, (c) FT-IR spectra, and (d-f) XPS spectra of Cu_2O@NWNH after CA test.

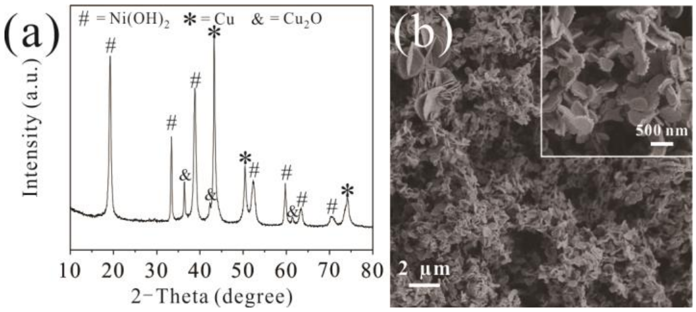

Figure S34. (a) XRD pattern and (b) SEM image of Cu_2O@NNH after CA test.

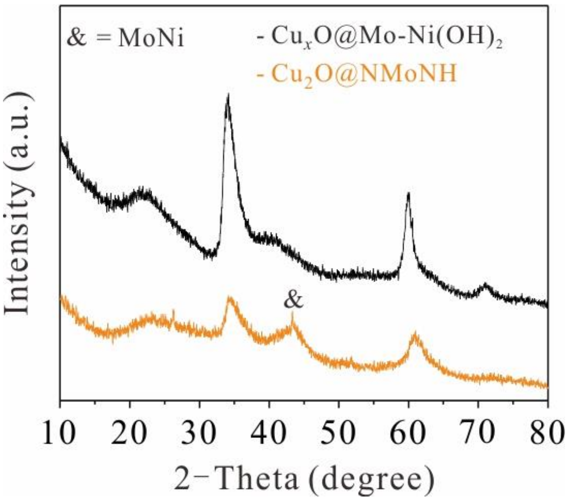

Figure S35. XRD patterns of Cu_xO@Mo-Ni(OH)$_2$ and Cu_2O@NMoNH.

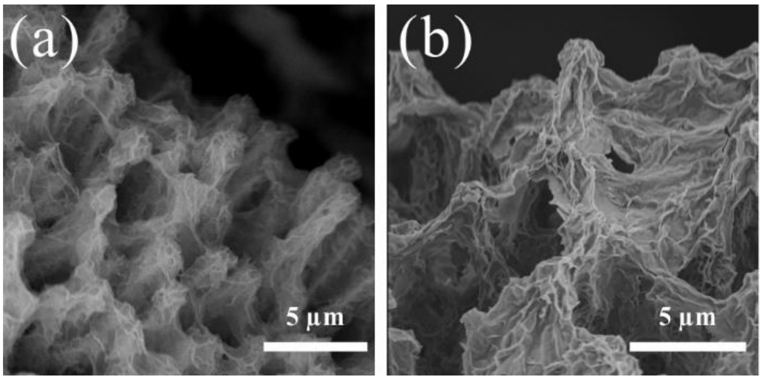

Figure S36. SEM images of (a) Cu_xO@Mo-Ni(OH)$_2$ and (b) Cu_2O@NMoNH.

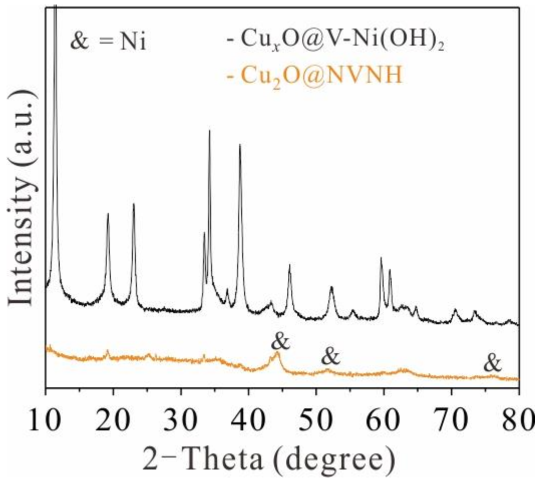

Figure S37. XRD patterns of Cu_xO@V-Ni(OH)$_2$ and Cu_2O@NVNH.

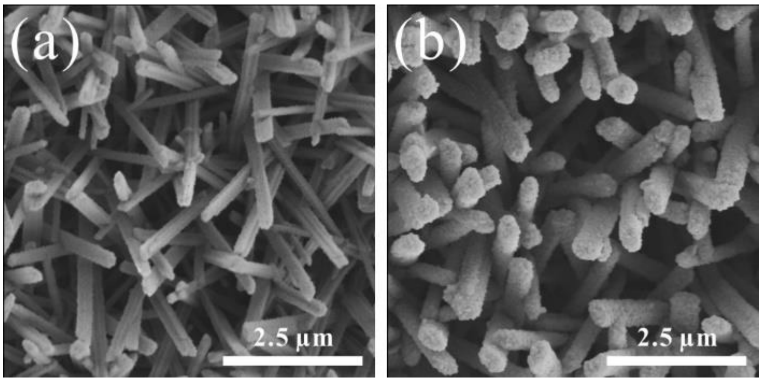

Figure S38. SEM images of (a) Cu_xO@V-Ni$(OH)_2$ and (b) Cu_2O@NVNH.

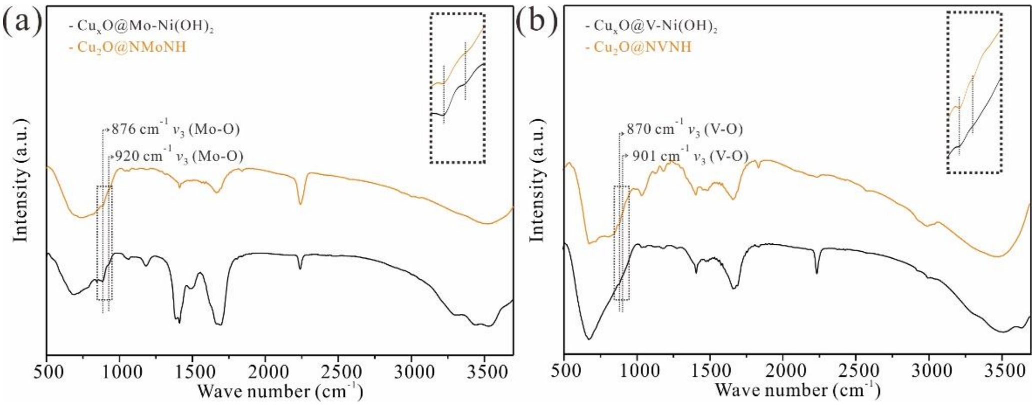

Figure S39. FT-IR spectra of Cu_xO@Mo-Ni$(OH)_2$, Cu_2O@NMoNH, Cu_xO@V-Ni$(OH)_2$, and Cu_2O@NVNH.

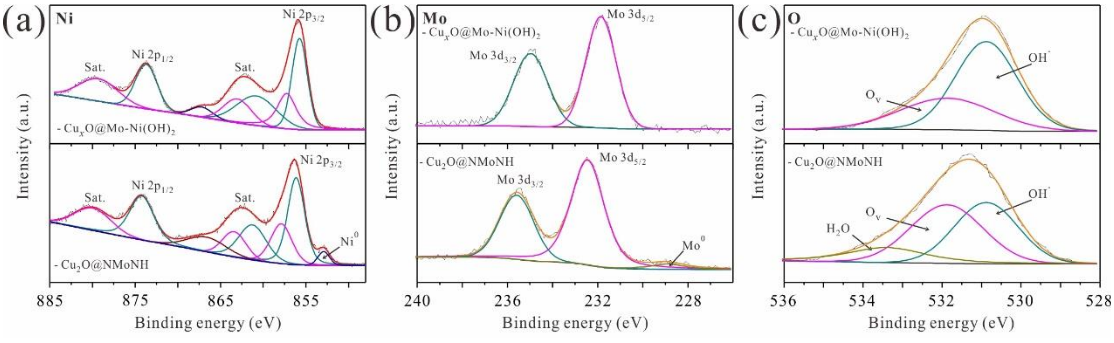

Figure S40. (a-c) The high-resolution Ni 2p (a), Mo 3d (b), and O 1s (c) XPS spectra of Cu_xO@Mo-Ni$(OH)_2$ and Cu_2O@NMoNH.

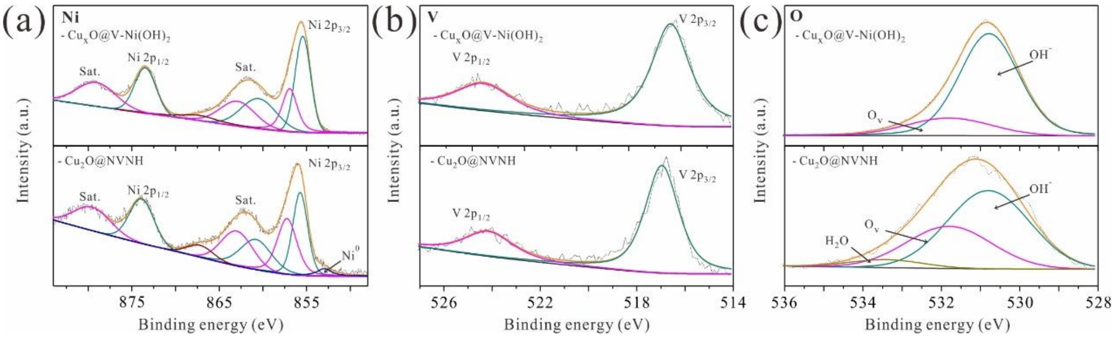

Figure S41. (a-c) The high-resolution Ni 2p (a), V 2p (b), and O 1s (c) XPS spectra of Cu_xO@V-$Ni(OH)_2$ and Cu_2O@NVNH.

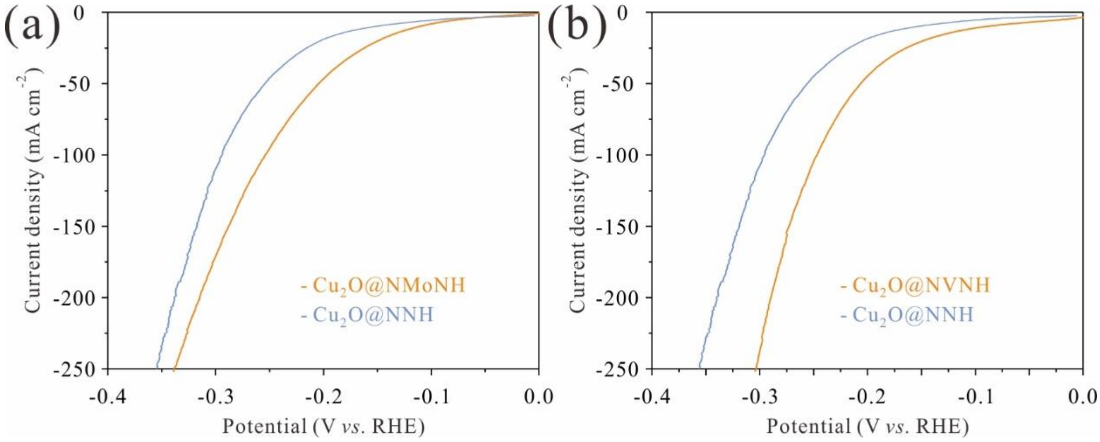

Figure S42. LSV curves of Cu_2O@NNH, Cu_2O@NMoNH, and Cu_2O@NVNH.

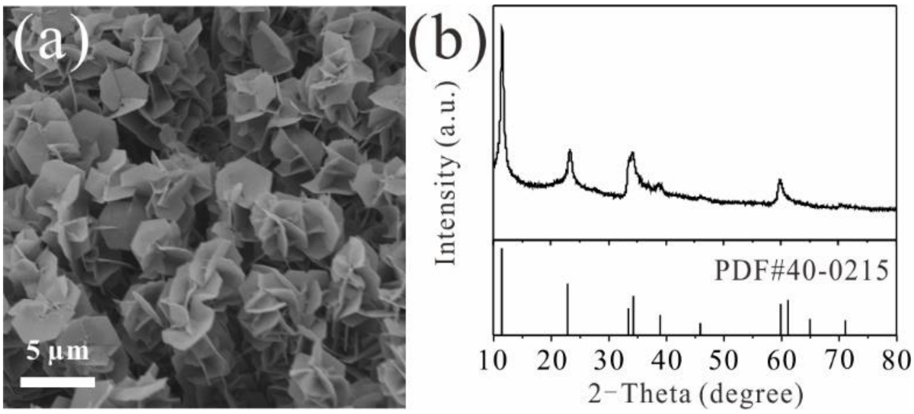

Figure S43. (a) SEM image and (b) XRD pattern of Cu_xO@NiFe LDH.

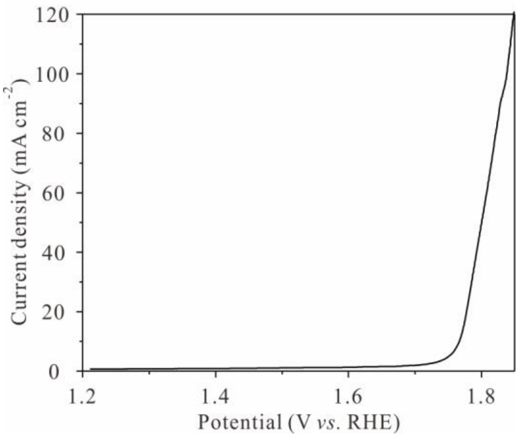

Figure S44. LSV curve of Cu_xO@NiFe LDH for OER in 1.0 M PBS.

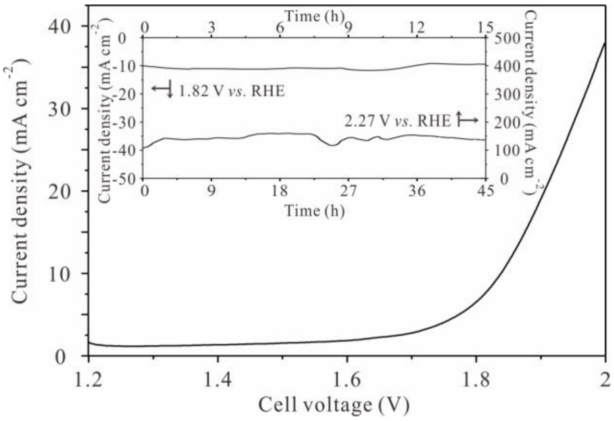

Figure S45. Overall water splitting performance of Cu_2O@NWNH//Cu_xO@NiFe LDH. The inset: CA tests for the assembled electrolysis cell.

***Table S1*.** Bond length in the structure of NNH and NWNH.

Structure	**C-O (Å)**	**W-O (Å)**	**Ni-O (inner) (Å)**	**Ni-O (outer) (Å)**	**Average Distance between Ni and $Ni(OH)_2$ ($Ni-Ni_{Ni(OH)_2}$) (Å)**
NNH	1.45	/	2.11 (Ni-O-C)	2.07	4.16
NWNH	1.46	1.92	2.07 (Ni-O-W)	2.08	4.03

Table S2. The 2θ and full width at half maxima (FWHM) of $Ni(OH)_2\cdot 0.75H_2O$ (003), $Ni(OH)_2$ (001) and $Ni(OH)_2\cdot 0.75H_2O$ (006) in $Ni(OH)_2$, W-5%-$Ni(OH)_2$, W-$Ni(OH)_2$ and W-20%-$Ni(OH)_2$.

	$Ni(OH)_2\cdot 0.75H_2O$ (003)		**$Ni(OH)_2$ (001)**		**$Ni(OH)_2\cdot 0.75H_2O$ (006)**	
	2θ (degree)	FWHM (degree)	2θ (degree)	FWHM (degree)	2θ (degree)	FWHM (degree)
$Ni(OH)_2$	11.37	0.29	19.20	0.373	23.00	0.355
W 5 %-$Ni(OH)_2$	11.41	0.432	19.23	0.503	23.04	0.478
W-$Ni(OH)_2$	11.27	0.56	19.16	0.605	22.95	0.542
W 20 %-$Ni(OH)_2$	11.22	0.543	19.33	0.629	22.85	0701

Table S3. The detailed values of fitted results in Figure. 4c, R_s: resistivity of solution; CPE-T: Constant phase element – T; CPE-P: Constant phase element – P; R_{ct}: resistivity of charge transfer

Sample	**Element**	**Value**
NNH	R_s	3.464
	CPE-T	0.0030562
	CPE-P	0.86962
	R_{ct}	51.78
NWNH	R_s	3.307
	CPE-T	0.013839
	CPE-P	0.8869
	R_{ct}	45.6

Table S4. Inductively coupled plasma–mass spectrometry (ICP-MS) results for $Ni(OH)_2$, W-$Ni(OH)_2$, Cu_xO@W-$Ni(OH)_2$, Cu_2O@NWNH, and Cu_2O@NWNH after *i-t* test.

Samples	**Ni (mmol/L)**	**W (mmol/L)**	**W/Ni**
W-$Ni(OH)_2$	1.015	0.098	9.7
Cu_xO@W-$Ni(OH)_2$	0.472	0.065	13.7
Cu_2O@NWNH	0.353	0.028	7.9
Cu_2O@NWNH after *i-t* test	0.290	0.039	13.4

Table S5. Comparison of HER performance of the Cu_2O@NWNH electrocatalyst with other reported catalysts in 1.0 M PBS.

Electrocatalysts	**Current density ($mA\ cm^{-2}$)**	**Overpotential (mV)**	**Tafel slope ($mV\ dec^{-1}$)**	**Stability (h)**	**Ref.**
Cu_2O@ NWNH	**10** **100**	**39** **150**	**37.2**	**48** **24**	**This work**
Pt-Co(OH)$_2$	10 100	84 253	/	/ /	8
np-$Co_9S_4P_4$	10 100	87 174	51	100 /	9
CoP/Co-MOF	10 50	49 ≈110	63	/ ≈17	10
$Ni_{0.1}Co_{0.9}P$	10	125	103	≈20	11
CoMoNiS-NF-31	10	117	56	≈20	12
$Ir_{0.5}W_{0.5}$	10	35	59.3	≈8	13
Ni-SP	10 100	38 214	27	10 /	14
PMFCP	10	117	/	/	15
CoW(OH)$_x$	10 20	73.6 114.9	149.59	/ 70	16
CrO$_x$/Cu-Ni	10 30	48 ≈100	64	/ ≈28	17
VN@N_3N-Ni-6	10 100	85 295	97	40	18
Co-P@PC-850	10	85	49	20	19
Fe-CoP	10	134	50.1	10	20
CoP_3/CoMoP-5	10	89	96.5	20	21

Table S6. Comparison of overall water splitting performance of Cu_2O@NWNH//Cu_xO@NiFe LDH with other reported electrocatalysts in 1.0 M PBS.

Electrocatalysts	**Current density ($mA\ cm^{-2}$)**	**Cell voltage (V)**	**Stability (h)**	**Ref.**
Cu_2O@NWNH// Cu_xO@NiFe LDH	**10** **100**	**1.82** **2.27**	**45** **15**	**This work**
CoP NA//CoP NA	10	1.92	10	22
$Ni_{0.1}Co_{0.9}P$//$Ni_{0.1}Co_{0.9}P$	10	1.89	20	11
CoMoNiS-NF-31// CoMoNiS-NF-31	10	1.8	20	12
$Ni(S_{0.5}Se_{0.5})_2$//$Ni(S_{0.5}Se_{0.5})_2$	10	1.87	12	23
S-$NiFe_2O_4$//S-$NiFe_2O_4$	10	1.95	24	24
CoO/$CoSe_2$//CoO/$CoSe_2$	10	2.18	10	25

REFERENCES

1. Wang, D.; Li, J.; Zhao, Y.; Xu, H. T.; Zhao, J. Z., Bifunctional Cu2Se-Co(OH)(2) nanotube array/Cu foam electrocatalyst for overall water splitting. *Electrochim. Acta* 2019, 316, 8-18.
2. Tang, Y.; Liu, Q.; Dong, L.; Wu, H. B.; Yu, X.-Y., Activating the hydrogen evolution and overall water splitting performance of NiFe LDH by cation doping and plasma reduction. *"Appl. Catal., B"* 2020, 266, 118627.
3. Kresse, G.; Joubert, D., From ultrasoft pseudopotentials to the projector augmented-wave method. *Physical Review B* 1999, 59, 1758-1775.
4. Perdew, J. P.; Burke, K.; Ernzerhof, M., Generalized gradient approximation made simple. *Phys. Rev. Lett.* 1996, 77, 3865-3868.
5. J. K. Nørskov, J. R., A. Logadottir, and L. Lindqvist Origin of the Overpotential for Oxygen Reduction at a Fuel-Cell Cathode. *J. Phys. Chem. B* 2004, 108, 17886-17892.
6. Sarkar, A.; Pramanik, S.; Achariya, A.; Pramanik, P., A novel sol-gel synthesis of mesoporous ZrO2-MoO3/WO3 mixed oxides. *Microporous Mesoporous Mater.* 2008, 115, 426-431.
7. Xue, X. Y.; Yu, F.; Peng, B. H.; Wang, G.; Lv, Y.; Chen, L.; Yao, Y. B.; Dai, B.; Shi, Y. L.; Guo, X. H., One-step synthesis of nickel-iron layered double hydroxides with tungstate acid anions via flash nano-precipitation for the oxygen evolution reaction. *Sustainable Energy Fuels* 2019, 3, 237-244.
8. Seh, Z. W.; Kibsgaard, J.; Dickens, C. F.; Chorkendorff, I. B.; Norskov, J. K.; Jaramillo, T. F., Combining theory and experiment in electrocatalysis: Insights into materials design. *Science* 2017, 355.
9. Tan, Y. W.; Luo, M.; Liu, P.; Cheng, C.; Han, J. H.; Watanabe, K.; Chen, M. W., Three-Dimensional Nanoporous Co9S4P4 Pentlandite as a Bifunctional Electrocatalyst for Overall Neutral Water Splitting. *ACS Appl. Mater. Interfaces* 2019, 11, 3880-3888.
10. Liu, T.; Li, P.; Yao, N.; Cheng, G. Z.; Chen, S. L.; Luo, W.; Yin, Y. D., CoP-Doped MOF-Based Electrocatalyst for pH-Universal Hydrogen Evolution Reaction. *Angew Chem Int Edit* 2019, 58, 4679-4684.
11. Wu, R.; Xiao, B.; Gao, Q.; Zheng, Y. R.; Zheng, X. S.; Zhu, J. F.; Gao, M. R.; Yu, S. H., A Janus Nickel Cobalt Phosphide Catalyst for High-Efficiency Neutral-pH Water Splitting. *Angew Chem Int Edit* 2018, 57, 15445-15449.
12. Yang, Y.; Yao, H. Q.; Yu, Z. H.; Islam, S. M.; He, H. Y.; Yuan, M. W.; Yue, Y. H.; Xu, K.; Hao, W. C.; Sun, G. B.; Li, H. F.; Ma, S. L.; Zapol, P.; Kanatzidis, M. G., Hierarchical Nanoassembly of MoS2/Co9S8/Ni3S2/Ni as a Highly Efficient Electrocatalyst for Overall Water Splitting in a Wide pH Range. *J. Am. Chem. Soc.* 2019, 141, 10417-10430.
13. Fu, L.; Hu, X.; Li, Y.; Cheng, G.; Luo, W., IrW nanobranches as an advanced electrocatalyst for pH-universal overall water splitting. *Nanoscale* 2019, 11, 8898-8905.
14. Abdullah, M. I.; Hameed, A.; Zhang, N.; Ma, M., Nickel Nanocrystal Assemblies as Efficient Electrocatalysts for Hydrogen Evolution from pH-Neutral Aqueous Solution. *ChemElectroChem* 2019, 6, 2100-2106.
15. Liu, H.; Peng, X.; Liu, X.; Qi, G.; Luo, J., Porous Mn-Doped FeP/Co3 (PO4)2 Nanosheets as Efficient Electrocatalysts for Overall Water Splitting in a Wide pH Range. *ChemSusChem* 2019, 12, 1334-1341.
16. Zhang, L.; Liu, P. F.; Li, Y. H.; Wang, C. W.; Zu, M. Y.; Fu, H. Q.; Yang, X. H.; Yang, H. G., Accelerating Neutral Hydrogen Evolution with Tungsten Modulated Amorphous Metal Hydroxides.

ACS Catal. 2018, 8, 5200-5205.

17. Dinh, C. T.; Jain, A.; de Arquer, F. P. G.; De Luna, P.; Li, J.; Wang, N.; Zheng, X. L.; Cai, J.; Gregory, B. Z.; Voznyy, O.; Zhang, B.; Liu, M.; Sinton, D.; Crumlin, E. J.; Sargent, E. H., Multi-site electrocatalysts for hydrogen evolution in neutral media by destabilization of water molecules. *Nat. Energy* 2019, 4, 107-114.

18. Dong, X.; Yan, H. J.; Jiao, Y. Q.; Guo, D. Z.; Wu, A. P.; Yang, G. C.; Shi, X.; Tian, C. G.; Fu, H. G., 3D hierarchical V-Ni-based nitride heterostructure as a highly efficient pH-universal electrocatalyst for the hydrogen evolution reaction. *J. Mater. Chem. A* 2019, 7, 15823-15830.

19. Wu, J.; Wang, D.; Wan, S.; Liu, H.; Wang, C.; Wang, X., An Efficient Cobalt Phosphide Electrocatalyst Derived from Cobalt Phosphonate Complex for All-pH Hydrogen Evolution Reaction and Overall Water Splitting in Alkaline Solution. *Small* 2019, e1900550.

20. Du, Y.; Wang, Z.; Li, H.; Han, Y.; Liu, Y.; Yang, Y.; Liu, Y.; Wang, L., Controllable synthesized CoP-MP (M=Fe, Mn) as efficient and stable electrocatalyst for hydrogen evolution reaction at all pH values. *Int. J. Hydrogen Energy* 2019, 44, 19978-19985.

21. Jiang, D.; Xu, Y.; Yang, R.; Li, D.; Meng, S.; Chen, M., CoP3/CoMoP Heterogeneous Nanosheet Arrays as Robust Electrocatalyst for pH-Universal Hydrogen Evolution Reaction. *ACS Sustainable Chem. Eng.* 2019, 7, 9309-9317.

22. Tingting Liu, L. X., Jianhui Yang, Rongmei Kong, Gu Du, Abdullah M. Asiri, Xuping Sun, and Liang Chen, Self-Standing CoP Nanosheets Array: AThree-Dimensional Bifunctional Catalyst Electrode for Overall Water Splitting in both Neutral and Alkaline Media. *ChemElectroChem* 2017, 4, 1840-1845.

23. Zeng, L.; Sun, K.; Chen, Y.; Liu, Z.; Chen, Y.; Pan, Y.; Zhao, R.; Liu, Y.; Liu, C., Neutral-pH overall water splitting catalyzed efficiently by a hollow and porous structured ternary nickel sulfoselenide electrocatalyst. *J. Mater. Chem. A* 2019, 7, 16793-16802.

24. Liu, J.; Zhu, D.; Ling, T.; Vasileff, A.; Qiao, S.-Z., S-NiFe2O4 ultra-small nanoparticle built nanosheets for efficient water splitting in alkaline and neutral pH. *Nano Energy* 2017, 40, 264-273.

25. Li, K.; Zhang, J.; Wu, R.; Yu, Y.; Zhang, B., Anchoring CoO Domains on CoSe2 Nanobelts as Bifunctional Electrocatalysts for Overall Water Splitting in Neutral Media. *Adv Sci (Weinh)* 2016, 3, 1500426.